Engineering 5 (2019) 568–575

Contents lists available at ScienceDirect

Engineering

journal homepage: www.elsevier.com/locate/eng

Research
Engines and Fuels—Article

Evaluation of H_2 Influence on the Evolution Mechanism of NO_x Storage and Reduction over Pt–Ba–Ce/γ-Al_2O_3 Catalysts

Pan Wang *, Jing Yi, Chuan Sun, Peng Luo, Lili Lei

School of Automotive and Traffic Engineering, Jiangsu University, Zhenjiang 212013, China

ARTICLE INFO

Article history:
Received 17 April 2018
Revised 20 August 2018
Accepted 15 February 2019
Available online 19 April 2019

Keywords:
Pt–Ba–Ce/γ-Al_2O_3 catalysts
Physicochemical properties
NO_x storage and reduction
NO_x emission
H_2 reductant

ABSTRACT

In this investigation, Pt–Ba–Ce/γ-Al_2O_3 catalysts were prepared by incipient wetness impregnation and experiments were performed to evaluate the influence of H_2 on the evolution mechanism of nitrogen oxides (NO_x) storage and reduction (NSR). The physical and chemical properties of the Pt–Ba–Ce/γ-Al_2O_3 catalysts were studied using a combination of characterization techniques, which showed that PtO_x, CeO_2, and $BaCO_3$, whose peaks were observed in X-ray diffraction (XRD) spectra, dispersed well on the γ-Al_2O_3, as shown by transmission electron microscope (TEM), and that the difference between Ce^{3+} and Ce^{4+}, as detected by X-ray photoelectron spectroscopy (XPS), facilitated the migration of active oxygen over the catalyst. In the process of a complete NSR experiment, the NO_x storage capability was greatly enhanced in the temperature range of 250–350 °C, and reached a maximum value of 315.3 $\mu mol \cdot g_{cat}^{-1}$ at 350 °C, which was ascribed to the increase in NO_2 yield. In a lean and rich cycling experiment, the results showed that NO_x storage efficiency and conversion were increased when the time of H_2 exposure (i.e., 30, 45, and 60 s) was extended. The maximum NO_x conversion of the catalyst reached 83.5% when the duration of the lean and rich phases was 240 and 60 s, respectively. The results revealed that increasing the content of H_2 by an appropriate amount was favorable to the NSR mechanism due to increased decomposition of nitrate or nitrite, and the refreshing of trapping sites for the next cycle of NSR.

1. Introduction

Compared with conventional stoichiometric engines, lean-burn engines such as lean-burn gasoline or diesel engines provide higher fuel efficiency and produce lower carbon dioxide (CO_2) emissions. However, the nitrogen oxides (NO_x, referring to nitric oxide (NO) and nitrogen dioxide (NO_2)) emitted from lean-burn engines render traditional three-way catalysts (TWCs) ineffective due to the ample oxygen (O_2) presence in the exhaust gas. Therefore, two promising de-NO_x technologies for the abatement of NO_x emissions—namely, selective catalytic reduction and NO_x storage and reduction (NSR), which were initially proposed by Toyota researchers in the 1990s—have been employed to meet regulations [1,2]. NSR catalysts mainly consist of alkali or alkaline earth metals (e.g., BaO and CeO_2) for NO_x storage, and noble metals such as rhodium (Rh) and platinum (Pt) that are well dispersed on a support such as alumina (Al_2O_3), which possesses a high specific surface area. Many research papers are also reporting that other additives such as cerium oxide (CeO_2) effectively promote the stability and durability of catalysts. NSR technology periodically involves a regular long lean (oxidation) period and short rich (reduction) excursion. The NO existing in the exhaust gas is oxidized to NO_2 by the noble metals and is stored in the storage component in the form of nitrites or nitrates during the lean phase. In rich atmospheres, reductants such as hydrogen (H_2), carbon monoxide (CO), propene (C_3H_6), and so forth are introduced into the exhaust gas, leading to the decomposition of the nitrites or nitrates into NO_x, which is subsequently reduced to nitrogen (N_2) on the noble metal sites [3].

With the aim of obtaining high NO_x conversions, numerous studies have been conducted on the optimization of catalytic formulations and operation conditions [4–11]. Traditional NSR catalysts are in the form of Pt–Ba/γ-Al_2O_3; however, the utilization of CeO_2 in recent studies has revealed the excellent abilities of this catalyst. CeO_2 favors NO_x storage efficiency (NSE) as a stored NO_x species, facilitates steam reforming reactions and water–gas reactions, and it stabilizes on a high dispersion of noble metals [12]. CeO_2-containing catalytic formulations have been proposed in which CeO_2 is used as a support because of its known capability

* Corresponding author.
E-mail address: wangpan@ujs.edu.cn (P. Wang).

https://doi.org/10.1016/j.eng.2019.02.005

in NO_x storage related to nitrate and nitrite species [13–15]. The action of CeO_2 as a promoter has also been thoroughly investigated. Le Phuc et al. [16] prepared a series of $Pt/Ba/Ce/Al_2O_3$ catalysts with different cerium/barium (Ce/Ba) molar ratios and found that the presence of Ce increased the NO_x conversion rate to some extent. Recent papers have focused on NSR conditions, including the effects of reductant type, reductant amount, and different lean and rich durations [17,18]. In terms of reductant types, Masdrag and coworkers [19] investigated the effect of H_2, CO, C_3H_6, and $H_2 + CO + C_3H_6$ on the NO_x conversion rate over $Pt/10\%BaO/Al_2O_3$. The results showed that H_2 was a superior reductant in the testing temperature range of 200–400 °C, obtaining a maximum conversion rate of 78% at 400 °C; this finding was similar to observations reported by Abdulhamid and coworkers [20]. The influence of the lean and rich durations on NSR was also studied. AL-Harbi and Epling [18] examined different regeneration protocols in the temperature window from 200 to 500 °C over a model NSR catalyst. The results revealed an obvious improvement in catalyst performance in the wake of increasing regeneration times at 200, 300, and 400 °C. In addition, Ansari et al. [21–24] synthesized $CoTiO_3/CoFe_2O_4$ nanostructures via a sol–gel auto-combustion technique and found evenly distributed spherical nanoparticles in X-ray diffraction (XRD) patterns and energy dispersive spectroscopy (EDS) patterns when the molar ratio of cobalt/titanium (Co/Ti) was 1:1. Mahdiani et al. [23,24] prepared $PbFe_{12}O_{19}$ nanostructures using sol–gel auto-combustion, and found the valine for the nanostructures to be 5123 Oe.

The objective of the present study was to optimize NSR capabilities in order to gain a higher NO_x conversion based on simulated gas tests, and to investigate the roles of temperature variances and the scale time of H_2 on the evolution mechanism of NSR during a complete NSR process and a cycle-average NSR process over the Pt–Ba–Ce/γ-Al_2O_3 (denoted herein as PBCA) catalyst, respectively. The catalyst was prepared by incipient wetness impregnation and was then characterized in terms of Pt dispersion, XRD, morphology and size of the catalyst, transmission electron microscope (TEM), surface chemical composition oxidation state, and X-ray photoelectron spectroscopy (XPS) in order to study the physicochemical properties of the catalyst.

2. Experimental procedure

2.1. Catalyst preparation

A series of PBCA catalysts were prepared by incipient wetness impregnation. First, γ-Al_2O_3 (Umicore) was impregnated in $Ce(NO_3)_2{\cdot}6H_2O$ solution (AR, Sinopharm Chemical Reagent Co., Ltd., China) to give a Ce loading of 15 wt%. $Ba(O_2CCH_3)_2$ (AR, Sinopharm Chemical Reagent Co., Ltd., China) as a precursor was subsequently incorporated into the sample using the same method, with a nominal Ba loading of 10 wt%. The sample was dried at 120 °C for 24 h and calcined at 550 °C in the air for 5 h. $H_2PtCl_6{\cdot}6H_2O$ (AR, Sinopharm Chemical Reagent Co., Ltd., China) was dissolved in deionized water and subjected to ultrasonic concussion for 30 min in order to obtain a homogeneous dispersion solution; it was then added to the abovementioned sample to gain Pt loadings of 0.285%, 0.577%, and 0.855%, respectively. After each impregnation, the sample was dried and calcined under the same conditions described above. Finally, the ball-milled sample was sieved using 40–60 mesh before the NSR experiment.

2.2. Catalyst characterization

XRD of the as-prepared sample was measured on a Bruker D8 Advance X-ray diffractometer with a nickel (Ni)-filtered copper (Cu) Kα (λ = 0.154068 nm) radiation source at 40 kV and 40 mA. Powder XRD patterns were recorded at 0.02° intervals in the range of 20°–80° with a scanning velocity of 7°·min^{-1}. Jade software (Jade Software Co., Ltd., New Zealand) was used for data treatment; identification of the crystalline phrase was performed using Joint Committee on Powder Diffraction Standards (JCPDS) cards. TEM was performed using a FEI Tecnai 12 electron microscope (Thermo Fisher Scientific Inc., USA) operating with a 120 kV accelerating voltage. Before being imaged, the powder sample was finely ground and dispersed ultrasonically in anhydrous ethanol at room temperature; a drop of the suspension was then dropped onto a lacey carbon-coated Cu grid of 200 mesh. XPS analysis was carried out on an ESCALAB™ 250Xi spectrometer from Thermo Fisher Scientific fitted with a micro-focused, monochromatic aluminum (Al) Kα source ($h\upsilon$ = 1486.6 eV), with a base pressure of about 5×10^{-14} MPa; the binding energies were referenced to the C 1s line at 284.6 eV from adventitious carbon.

2.3. Catalyst activities evaluation

The lab apparatus for the NSR experiments is shown in Fig. 1. The apparatus was composed of a reactor, gas paths, a gas paths control part, and a gas analyzer. The catalyst evaluation was carried out with 0.3 mL (0.40 g) of catalyst using a fixed-bed quartz micro-reactor with an inside diameter of 10 mm. The catalyst was placed inside a tubular electric resistance furnace, the temperature of which was controlled by a thermocouple dipped into the catalyst bed. The catalyst was plugged in and sandwiched between two silica wool layers to prevent the sample from moving away. The gas paths and the gas paths control part included gas cylinders, reducing valves, valve controllers, and mass-flow controllers. All gases were introduced by mass-flow controllers with a total flow rate of 280 mL·min^{-1}, giving a space velocity of 5.6×10^4 h^{-1}. The outlet NO_x (NO and NO_2) concentration was detected by a NO_x analyzer (Thermo Scientific™ Model 42*i*-HL, Thermo Fisher Scientific Inc., USA). In our study, prior to completing the NSR experiments, the catalyst sample temperature was increased (20 °C·min^{-1}) to 450 °C in N_2 and was then exposed to a regeneration gas mixture consisting of 1% H_2 and a balance of N_2 for 30 min. The catalyst was then cooled to the required measurement temperature in N_2, and the reaction temperature was varied from 250 to 400 °C. When cycling the NSR experiments performed at 350 °C, a fixed 240 s lean phase and varied rich phase (30, 45, and 60 s) were used. The NO_x conversion was based on the average of two cycles when a steady cycle-to-cycle performance was achieved. The gas composition and parameters used for completing and cycling the NSR experiments are summarized in Table 1.

The activity of the catalyst sample during the lean and rich periods was evaluated by the following formula. The NO_x storage capacity (NSC) was defined as follows:

$$\mathrm{NSC} = \frac{\int_0^{t_L} (f_{\mathrm{NO,in}} - f_{\mathrm{NOx,out}})\mathrm{d}t}{m_{\mathrm{cat}}} \quad (1)$$

where $f_{\mathrm{NO,in}}$ is the NO molar flow (mol·min^{-1}) at the inlet, $f_{\mathrm{NOx,out}}$ is the NO_x molar flow at the outlet, t_L is the duration of the lean phase, and m_{cat} is the mass of the catalyst (g).

The cycle-average NO_x reduction conversion was based on two consecutive steady-state cycles, and the mean conversion was calculated according to the following formula:

$$\mathrm{NO}_{x,\mathrm{conversion}} = \frac{f_{\mathrm{NOx,in}} t_L - \int_0^t f_{\mathrm{NOx,out}}\mathrm{d}t}{f_{\mathrm{NOx,in}} t_L} \quad (2)$$

where t is the total cycle length.

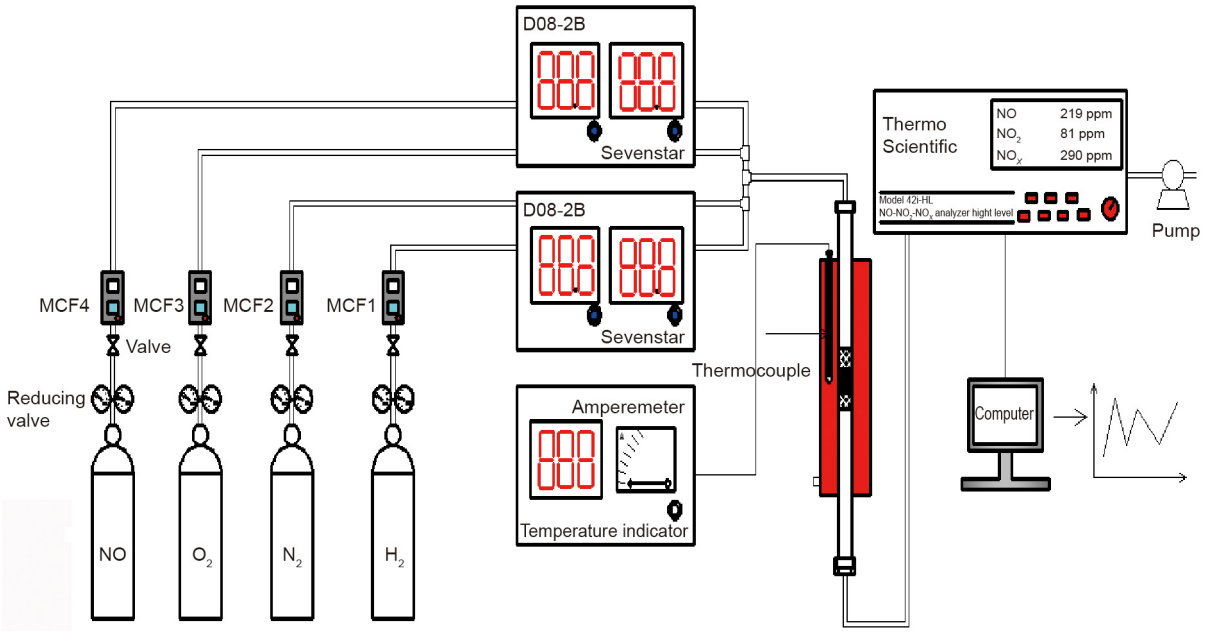

Fig. 1. Scheme of the lab apparatus for NSR experiments. MCF: mass flow meter.

Table 1
Details of flow conditions used in the complete NSR experiments and cycling NSR experiments.

Experiment type	Phase	Flow conditions					Reaction temperature (°C)	Time
		Space velocity (h^{-1})	NO content (ppm)	O_2 content	H_2 content	N_2 content		
Complete NSR	Lean	5.6×10^4	500	10%	0	10%	250, 300, 350, and 400	Till the spilled NO_x concentration is equal to the inlet NO concentration
Cycling NSR	Rich	5.6×10^4	0	0	1%	1%	350	Till outlet NO_x concentration is equal to zero
	Lean	5.6×10^4	500	10%	0	10%		240 s
	Rich	5.6×10^4	0	0	1%	1%		30, 45, and 60 s

3. Results and discussion

3.1. Characterization of the catalyst

Fig. 2 shows the X-ray diffractograms of the PBCA catalysts. XRD spectra were taken on a freshly calcined sample. The XRD analysis showed that the main phase in PBCA was γ-Al_2O_3 (JCPDS No. 48-0366), which exhibited a typical cubic fluorite structure. The presence of $BaCO_3$ (JCPDS No. 05-0378) in the International Center for Diffraction Data (ICDD) database was observed, and was consistent with the decomposition of $Ba(O_2CCH_3)_2$ into crystalline $BaCO_3$ during catalyst calcination at 500 °C [25]. The peak of the $BaCO_3$ tended to decrease along with the increase of Pt content, and disappeared entirely when the Pt content was 0.855 wt%.

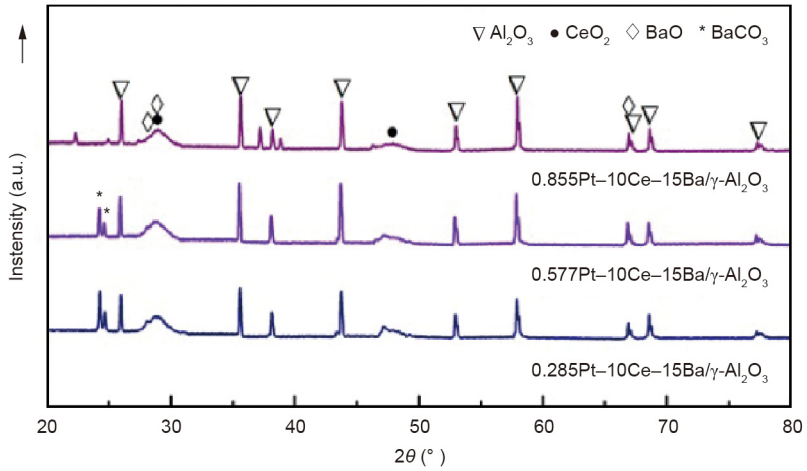

Fig. 2. XRD profiles of the PBCA samples. 2θ: scattering angle.

Neither Pt nor PtO_x were found in the XRD profile, which indicates that Pt exists as an amorphous or poorly crystalline phase monolayer, or else greatly disperses on the surface of the storage component and γ-Al_2O_3 and thus cannot easily be observed through XRD. The peaks belong to BaO when 2θ is equal to 28.04°, 28.68°, and 66.80°, and CeO_2 (JCPDS No. 43-1002) peaks emerge at the degrees of 28.68° and 47.02°.

Fig. 3 shows the TEM pattern, which was used to examine the morphology and size of the 0.577Pt–10Ce–15Ba/γ-Al_2O_3 catalyst. The TEM image reveals that there are many nanoparticles with sizes varying in the range of 1–5 nm on the catalyst (as indicated by the red circles), which can be assigned to Pt or PtO_x particles; this indicates that the Pt species is well dispersed, perhaps because of the strong interaction between Pt and CeO_2 [26]. The larger black particle in the image (indicated by the white circle) can be regarded as the aggregation of CeO_2 and $BaCO_3$. The light grey zone on which the PtO_x, CeO_2, and $BaCO_3$ are deposited can be regarded as γ-Al_2O_3.

XPS analysis was carried out to elucidate the surface chemical composition and oxidation state on the surface of the catalyst. The survey scan analysis was performed in a binding energy range between 0 and 1200 eV, and is presented in Fig. 4(a). The survey's spectrum shows that Ce, Ba, O, C, Pt, and Al are present on the 0.577Pt–10Ce–15Ba/γ-Al_2O_3 catalyst surface, and there are no obvious impurities present. The XPS spectrum of the chemical state of Ce is shown in Fig. 4(b). The complex Ce 3d level spectrum has spin–orbit doublets that are $3d_{5/2}$ and $3d_{3/2}$. The peaks V and U correspond to Ce $3d_{5/2}$ and Ce $3d_{3/2}$, respectively. In addition, the bands V (882.6 eV), V″ (889.2 eV), V‴ (898.4 eV), U (901.1 eV), U″ (906.9 eV), and U‴ (916.9 eV) refer to the presence of Ce^{4+}, and V′ (885.6 eV) and U′ (903.6 eV) are related to Ce^{3+}. These peaks clearly indicate that the Ce^{4+} oxidation state is predominant, while the peaks for Ce^{3+} are very weak. According to the spectrum areas, the ratio of Ce^{3+}/Ce^{4+} is 0.06. The binding energy of the Ba $3d_{5/2}$ core-level is 780.1 eV, suggesting that Ba is carbonated; this is consistent with the observation of the C 1s component near 280.9 eV, which is the fingerprint of carbonate structures. The narrow spectrum of O 1s, which is fitted into two peaks, is depicted in Fig. 4(c). The peak located at 529.1 eV (hereafter denoted as O_α) corresponds to the surface lattice oxygen species (O^{2-}) [27], of which a small contribution could be due to PtO_x species [28]. Moreover, the second peak at 531.2 eV (hereafter denoted as O_β) corresponds to the chemisorbed oxygen [29]. It has been reported that surface chemisorbed oxygen is the most active oxygen, playing an important role in the NO-to-NO_2 oxidation reaction [30,31]. For Pt, only the Pt $4d_{5/2}$ spectrum is recorded due to the peak of Pt 4f, which is overlapped by the Al 2p peak (74.1 eV) [32,33]. As can be seen in Fig. 4(d), a major peak at a lower binding energy (314.5 eV) is associated with metallic Pt (Pt^{0+}), and a minor one at higher position (316.8 eV) signifies the presence of oxidized Pt (PtO or PtO_2).

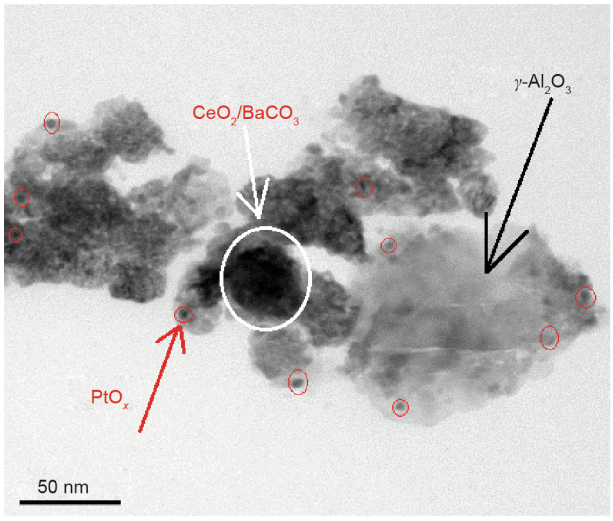

Fig. 3. TEM image of 0.577Pt–10Ce–15Ba/γ-Al_2O_3 catalyst.

3.2. Complete NO_x storage and reduction

In order to obtain a good understanding of the NSR process, a complete NSR experiment was conducted. The reaction was not switched to the rich phase until the spilled NO_x concentration was equal to the inlet NO concentration, and the next cycle was initiated only when the outlet NO_x concentration in the rich phase decreased to zero. The experiment was carried out at 250, 300, 350, and 400 °C using a continuously flowing mixture of 500 ppm NO, 10% O_2 and N_2 (in balance) in the lean phase, and 1% H_2 and N_2 (in balance) in the rich phase. The outlet NO_x ($NO + NO_2$) concentration value was obtained via a NO_x analyzer. Fig. 5 shows the evolution of NO_x ($NO + NO_2$) at the reactor during the complete NSR period at different temperatures. The results of the complete NSR experiments are summarized in Table 2. As shown in Fig. 5(a), when the experiment began (t = 0 min)—that is, when the gas mixtures were switched to lean compositions—the NO_x-containing mixture showed a delay of about 3 min, and the concentration then increased to the asymptotic values corresponding to the inlet concentration of 500 ppm NO. Of the NO_x, NO occurred initially, while NO_2 was also observed due to the oxidation of NO by O_2 on Pt or oxidized Pt sites via Reaction (3). As previously reported in the literature [34,35], NO_x molecules were absorbed at different Ba absorption sites; the most active component among these was BaO, although this mainly existed as $BaCO_3$ under real working conditions [36]. The overall reactions are given below, as Reactions (3) to (7):

$$2NO + O_2 \rightarrow 2NO_2 \quad (3)$$

$$2BaO + 4NO + 3O_2 \rightarrow 2Ba(NO_3)_2 \quad (4)$$

$$2BaCO_3 + 4NO + 3O_2 \rightarrow 2Ba(NO_3)_2 + 2CO_2 \quad (5)$$

$$BaO + 3NO_2 \rightarrow Ba(NO_3)_2 + NO \quad (6)$$

$$BaCO_3 + 3NO_2 \rightarrow Ba(NO_3)_2 + CO_2 + NO \quad (7)$$

Given the information in Fig. 5 and Table 2, it can be seen that the time required for complete NO_x storage was 41 min, the NSC was 119.8 $\mu mol \cdot g_{cat}^{-1}$, and the corresponding NSE was 18.7% at 250 °C. When the gas compositions were switched to the rich condition, it is worth noting that NO was quickly reduced to zero by H_2, while NO_2 showed a huge pulse to 650 ppm before quickly decreasing to zero (as clearly shown in the zoomed-in zone in Fig. 5(a)). The NO_x desorption peak area was mainly composed of NO_2, which indicates that NO_2 was more easily stored than NO. When H_2 was introduced, the surface adsorbing NO_x was quickly reduced and the exothermic reaction with NO_x caused the catalyst temperature to rise, accelerating the decomposition of the nitrate or nitrite. NO_x-removal efficiency is not only related to NSC in the lean phase, but is also concerned with the reduction of trapped NO_x during the rich phase; therefore, the released NO_x in the rich phase led to a decrease in the NO_x conversion (13.5%) compared with the NSE. When the temperature increased from 250 to 400 °C, the NO_x evolution curves were similar to those at 250 °C. However, the NSC was greatly enhanced in the range of 250–350 °C, despite a slight decrease at 400 °C, and attained the maximum value of 315.3 $\mu mol \cdot g_{cat}^{-1}$ at 350 °C, which is ascribed to the increase in NO_2 yield. Furthermore, the amount of NO_2 increased

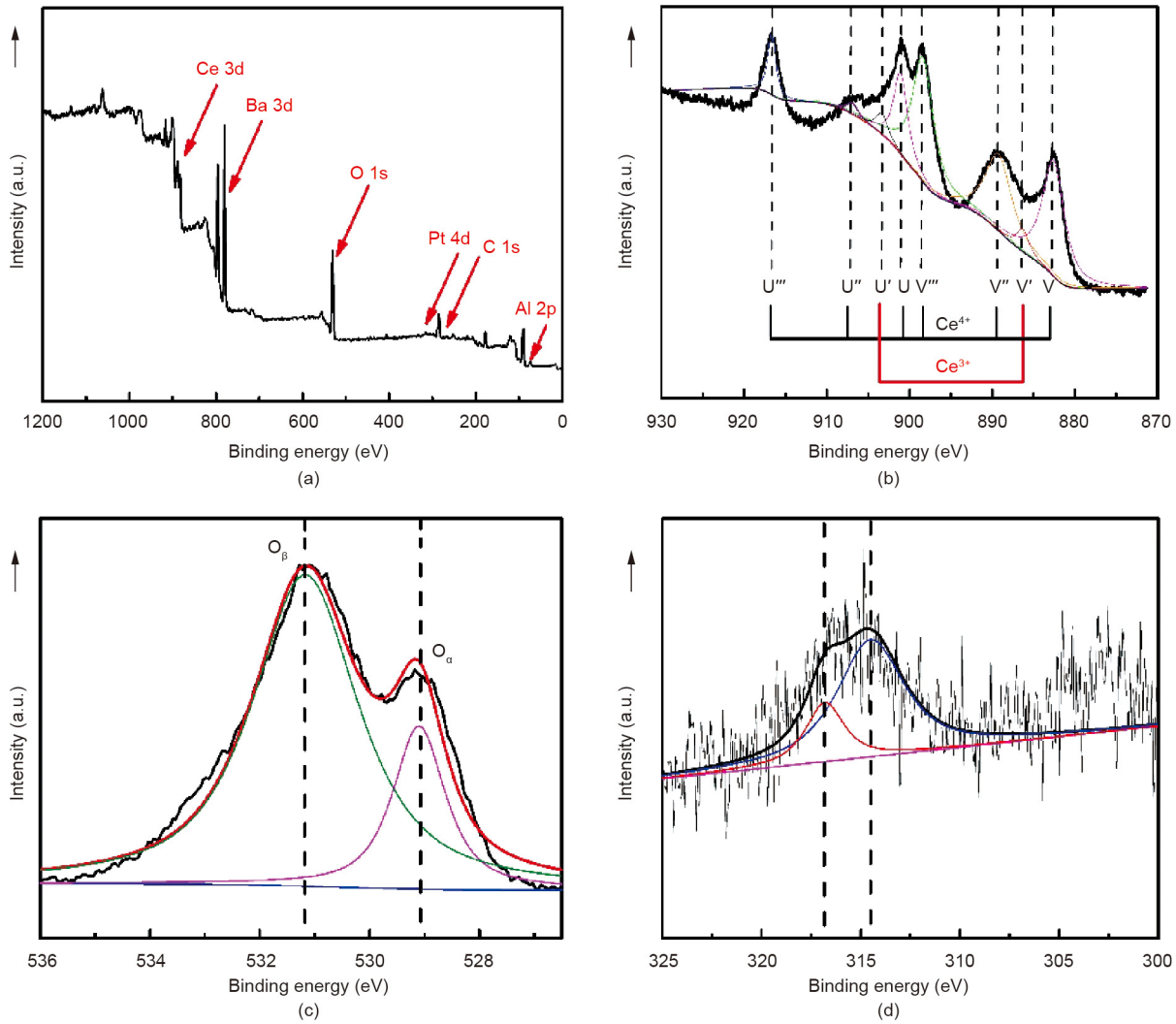

Fig. 4. XPS patterns of 0.577Pt–10Ba–15Ce/γ-Al_2O_3 catalyst: (a) Survey; (b) Ce 3d; (c) O 1s; (d) Pt 4d.

with temperature, and the NO_2/NO_x ratio increased from 0.09 to 0.59 in the temperature range of 250–400 °C. The NSC increase in the temperature range of 250–350 °C can be mainly attributed to the increased NO_2/NO_x ratio, with NO_2 being more favorably trapped on BaO sites as nitrates or nitrites than NO. At 400 °C, the NSC reached a value close to that observed at 350 °C, but the NO_2/NO_x was much higher (Table 2). These results indicate that higher temperatures accelerate the thermal decomposition of nitrates or nitrites in the NO_x storage process, and that the former predominates at higher temperatures, leading to decreased NSC. The catalyst reached its maximum NSC at 350 °C, much higher than that of 250 and 300 °C. However, the NO_x conversion for the whole testing temperature varied in a narrow range from 13.5% to 21.3%, as shown in Table 2.

Fig. 6 depicts the NSE as a function of the storage time at different temperatures. It is clear that the NSE decreases with storage time for all measured temperatures during the initial 5 min, the NSE for all temperatures is greater than 90%, and the maximum is 94.7% at 350 °C, indicating that almost all of the introduced NO during the initial lean phase is trapped by the catalyst. As the storage time reaches 40 min, the NSE drops to 22.5%, 28.5%, 42.9%, and 43.7% for 250, 300, 350, and 400 °C, respectively, which is due to the fact that the NO_x trapping sites are gradually reduced and eventually saturated. In actual application, a higher NSE is required to reduce more NO_x in order to meet the strict emission regulations. Using our proposed strategy to gain a better NO_x conversion, we optimized the experiment conditions by shortening the storage time to 4 min accompanied by a 30, 45, and 60 s rich-phase duration.

3.3. Cycling NO_x storage and reduction

As described above, the maximum NSC was obtained at 350 °C. To further study the real-world applications, a series of lean–rich cycling experiments was carried out at 350 °C by varying the rich-phase durations (30, 45, and 60 s) while maintaining the lean phase at 240 s. Fig. 7 depicts the evolution of NO_x in the outlet feed of the catalyst's initial 6–8 lean–rich cycles. The catalytic system reached a steady cycle-to-cycle performance after about five cycles. A summary of the results is provided in Table 3. As can be seen from the enlarged view of the steady cycles, NO_x was effectively trapped with very low emissions during the lean condition, and the NO_x emissions were stabilized at 116, 102, and 81 ppm for 240-lean/30-rich, 240-lean/45-rich, and 240-lean/60-rich conditions, respectively. The NO_x outlet concentrations were much lower than the NO feed concentration (500 ppm), indicating that NO_x can be effectively stored over the catalyst; the amounts of trapped NO_x were 112.6, 117.2, and 118.4 $\mu mol \cdot g_{cat}^{-1}$ for the 30, 45, and 60 s regeneration times, corresponding to an NSE of 90.0%, 93.4%, and 94.7%, respectively. Furthermore, for each

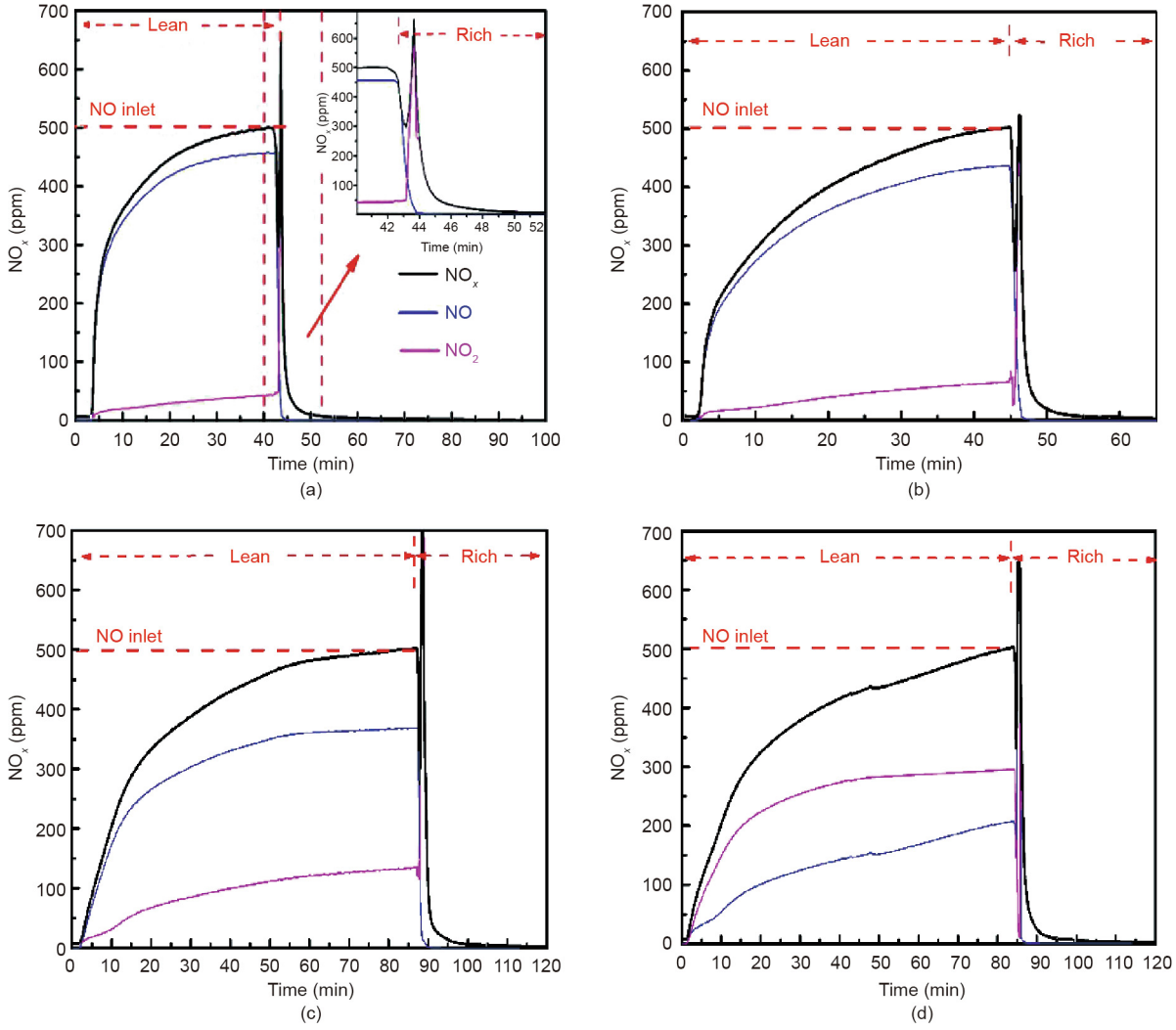

Fig. 5. Evolution of NO_x ($NO + NO_2$) at the reactor exit during the complete NSR period at different temperatures: (a) 250 °C; (b) 300 °C; (c) 350 °C; (d) 400 °C.

Table 2
Complete NSR measured at different temperatures.

Temperature (°C)	NO_2/NO_x	NSC ($\mu mol \cdot g_{cat}^{-1}$)	NSE (%)	NO_x conversion rate (%)
250	0.09	119.8	18.7	13.5
300	0.13	186.3	22.5	19.5
350	0.27	315.3	24.1	21.3
400	0.59	295.1	25.4	20.6

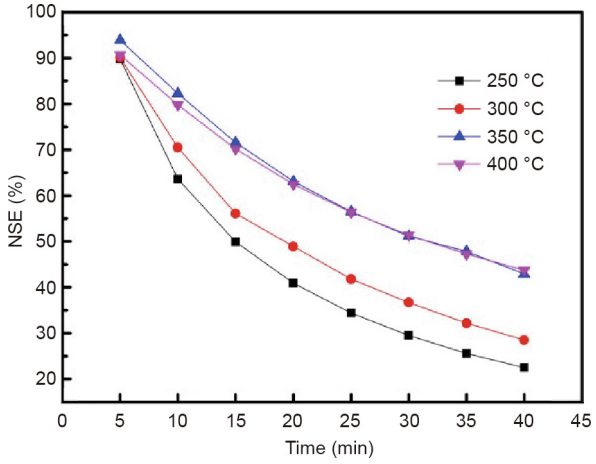

Fig. 6. NSE as a function of storage time at different temperatures.

experiment, NO_2 was observed during the lean phase of the cycling, revealing that NSE was not limited by the kinetics of NO oxidation. When the feed gases were switched to a rich condition, a sharp NO_x spike occurred, which can be determined indicating that the decomposition rate of the nitrates or nitrites (Reactions (8)–(10) [37,38]) was higher than the NO_x reduction rate (Reactions (11) and (12)), and that the NO_x conversion rate was limited by the reduction step.

$$2Ba(NO_3)_2 \leftrightarrow 2BaO + 4NO_2 + O_2 \quad (8)$$

$$2Ba(NO_3)_2 \leftrightarrow 2BaO + 4NO + 3O_2 \quad (9)$$

$$2Ba(NO_2)_2 \leftrightarrow 2BaO + 4NO + O_2 \quad (10)$$

$$2NO + 2H_2 \rightarrow 2H_2O + N_2 \quad (11)$$

$$2NO_2 + 4H_2 \rightarrow 4H_2O + N_2 \quad (12)$$

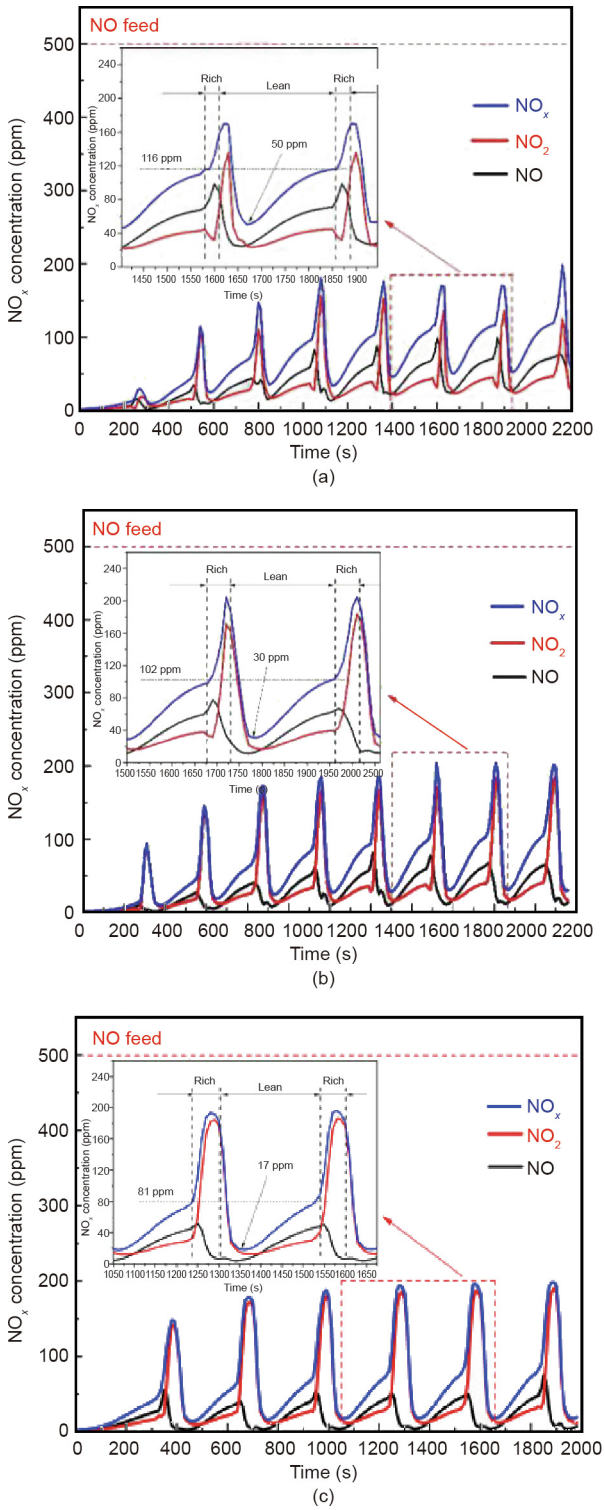

Fig. 7. NO_x concentration profiles during lean–rich cycling at 350 °C with a fixed 240 s lean phase and varied rich phase: (a) 30 s, (b) 45 s, and (c) 60 s.

Table 3
Cycling NSR measured at different rich phase time.

Lean, rich phase time	Trapped NO_x ($\mu mol \cdot g_{cat}^{-1}$)	NSE (%)	NO_x conversion rate (%)
240 s, 30 s	112.6	90.0	76.3
240 s, 45 s	117.2	93.4	80.4
240 s, 60 s	118.4	94.7	83.9

In addition, the amount of desorbed NO_x was significantly augmented, especially as unreduced NO_2 during the rich period steadily increased as the regeneration time extended. This finding was attributed to the amount of released NO_x that was a function of the NO_x trapped during the previous lean phase. As illustrated in Table 3, the amount of trapped NO_x increased when the regeneration time was prolonged. The NO_x rapidly decreased to a low level after that, but the degree of this reduction differed; for a 30 s rich-phase duration, the lowest NO_x was 50 ppm, but when the rich period was progressively lengthened to 45 s and then 60 s, the NO_x was reduced to a minimum of 30 and 17 ppm, respectively. This finding can be ascribed to the acquired H_2 amount increasing when the regeneration time was extended, which would lead to the NO_x stored in the catalyst previously being desorbed and restored more thoroughly, and which would provide more oxygen vacancies. Hence, the initial NO_x adsorption concentration in the next cycle decreased and superior catalytic performance was exhibited. However, the fuel consumption would be increased as the regeneration time extended under the practical conditions. It could be concluded that when the duration of the lean and rich phases was 240 and 60 s, respectively, the NSE and NO_x conversion rate reached the highest level. This finding reveals that prolonging the regeneration time appropriately is favorable due to the increased decomposition of nitrates or nitrites and the refreshing of trapping sites for the next cycle.

4. Conclusions

In this study, a PBCA catalyst prepared by incipient wetness impregnation was characterized by XRD, TEM, and XPS technologies in order to study its physical and chemical properties. Both complete and cycling NSR experiments were adopted to research the effect of H_2 on the evolution mechanism of NSR over the NSR catalyst. The results showed that each component of the catalyst was well-crystallized. The TEM image showed that the activity component—and especially PtO_x, which had a particle size in the 1–5 nm range—was equally dispersed on the γ-Al_2O_3. In addition, Ce existing with a Ce^{3+}/Ce^{4+} ratio of 0.06 facilitated the migration of active oxygen over the catalyst. In the complete NSR experiment, the NSC increase that occurred in the temperature range of 250–350 °C was mainly attributed to the increased NO_2/NO_x ratio due to NO_2 being more favorably trapped on BaO sites as nitrates or nitrites than NO. When the gas compositions were switched to the rich condition, NO was quickly reduced to zero by H_2, while NO_2 showed a huge pulse before decreasing to zero. In cycling NSR experiments at 350 °C, the results demonstrated that the NO_x conversion rate increased substantially in comparison with the complete NSR experiment. Furthermore, the NSE and conversion rate increased gradually when the regeneration time was extended (30, 45, and 60 s) due to the increased decomposition of nitrates or nitrites and the refreshment of trapping sites for the next cycle. The maximum NO_x conversion of the catalyst reached 83.5% when the duration of the lean and rich phases was 240 and 60 s, respectively, indicating that prolonging the regeneration time appropriately had a favorable result.

Acknowledgements

The authors wish to acknowledge financial support of this research by the National Natural Science Foundation of China (51676090), the Natural Science Foundation of Jiangsu Province (BK20150513), and the Six Talent Peaks Project in Jiangsu Province. The authors acknowledge the contribution of Professor Guanjun Qiao for technical support.

Compliance with ethics guidelines

Pan Wang, Jing Yi, Chuan Sun, Peng Luo, and Lili Lei declare that they have no conflict of interest or financial conflicts to disclose.

References

[1] Fridell E, Skoglundh M, Westerberg B, Johansson S, Smedler G. NO_x storage in barium-containing catalysts. J Catal 1999;183(2):196–209.
[2] Rico-Pérez V, García-Cortés JM, Bueno-López A. NO_x reduction to N_2 with commercial fuel in a real diesel engine exhaust using a dual bed of Pt/beta zeolite and RhO_x/ceria monolith catalysts. Chem Eng Sci 2013;104(50):557–64.
[3] Park S, Choi B, Kim H, Kim JH. Hydrogen production from dimethyl ether over Cu/γ-Al_2O_3 catalyst with zeolites and its effects in the lean NO_x trap performance. Int J Hydrogen Energy 2012;37(6):4762–73.
[4] Dai H. Environmental catalysis: a solution for the removal of atmospheric pollutants. Sci Bull 2015;60(19):1708–10.
[5] Wu W, Wang X, Jin S, Wang R. $LaCoO_3$ perovskite in Pt/$LaCoO_3$/K/Al_2O_3 for the improvement of NO_x storage and reduction performances. RSC Adv 2016;6(78):74046–52.
[6] Harold MP. NO_x storage and reduction in lean burn vehicle emission control: a catalytic engineer's playground. Curr Opin Chem Eng 2012;1(3):303–11.
[7] He X, Meng M, He J, Zou Z, Li X, Li Z, et al. A potential substitution of noble metal Pt by perovskite $LaCoO_3$ in $ZrTiO_4$ supported lean-burn NO_x trap catalysts. Catal Commun 2010;12(3):165–8.
[8] Rui Y, Zhang Y, Liu D, Meng M, Jiang Z, Zhang S, et al. A series of ceria supported lean-burn NO_x trap catalysts $LaCoO_3$/K_2CO_3/CeO_2 using perovskite as active component. Chem Eng J 2015;260:357–67.
[9] Perng CCY, Easterling VG, Harold MP. Fast lean-rich cycling for enhanced NO_x conversion on storage and reduction catalysts. Catal Today 2014;231(8):125–34.
[10] Kabin KS, Muncrief RL, Harold MP, Li Y. Dynamics of storage and reaction in a monolith reactor: lean NO_x reduction. Chem Eng Sci 2004;59(22):5319–27.
[11] Mei X, Wang J, Yang R, Yan Q, Wang Q. Synthesis of Pt doped Mg-Al layered double oxide/graphene oxide hybrid as novel NO_x storage-reduction catalyst. RSC Adv 2015;5(95):78061–70.
[12] Atribak I, Bueno-López A, García-García A. Combined removal of diesel soot particulates and NO_x over CeO_2–ZrO_2 mixed oxides. J Catal 2008;259(1):123–32.
[13] Casapu M, Grunwaldt JD, Maciejewski M, Baiker A, Eckhoff S, Gobel U, et al. The fate of platinum in Pt/Ba/CeO_2 and Pt/Ba/Al_2O_3 catalysts during thermal aging. J Catal 2007;251(1):28–38.
[14] Roy S, Baiker A. NO_x storage-reduction catalysis: from mechanism and materials properties to storage-reduction performance. Chem Rev 2009;109(9):4054–91.
[15] Caglar B, Uner D. NO oxidation and NO_x storage over Ce–Zr mixed oxide supported catalysts. Catal Commun 2011;12(6):450–3.
[16] Le Phuc N, Courtois X, Can F, Royer S, Marecot P, Duprez D. NO_x removal efficiency and ammonia selectivity during the NO_x storage-reduction process over Pt/BaO(Fe, Mn, Ce)/Al_2O_3 model catalysts. Part II: influence of Ce and Mn–Ce addition. Appl Catal B 2011;102(3):362–71.
[17] Lin S, Yang L, Yang X, Zhou R. Redox properties and metal-support interaction of Pd/$Ce_{0.67}Zr_{0.33}O_2$–Al_2O_3 catalyst for CO, HC and NO_x elimination. Appl Surf Sci 2014;305:642–9.
[18] AL-Harbi M, Epling WS. Effects of different regeneration timing protocols on the performance of a model NO_x storage/reduction catalyst. Catal Today 2010;151(3–4):347–53.
[19] Masdrag L, Courtois X, Can F, Duprez D. Effect of reducing agent (C_3H_6, CO, H_2) on the NO_x conversion and selectivity during representative lean/rich cycles over monometallic platinum based NSR catalysts. Influence of the support formulation. Appl Catal B 2014;146(5):12–23.
[20] Abdulhamid H, Fridell E, Skoglundh M. Influence of the type of reducing agent (H_2, CO, C_3H_6, and C_3H_8) on the reduction of stored NO_x in a Pt/BaO/Al_2O_3 model catalyst. Top Catal 2004;30(1–4):161–8.
[21] Ansari F, Sobhani A, Salavati-Niasari M. Simple sol–gel synthesis and characterization of new $CoTiO_3$/$CoFe_2O_4$ nanocomposite by using liquid glucose, maltose and starch as fuel, capping and reducing agents. J Colloid Interface Sci 2018;514:723–32.
[22] Amiri O, Mir N, Ansari F, Salavati-Niasari M. Design and fabrication of a high performance inorganic tandem solar cell with 11.5% conversion efficiency. Electrochim Acta 2017;252:315–21.
[23] Mahdiani M, Sobhani A, Ansari F, Salavati-Niasari M. Lead hexaferrite nanostructures: green amino acid sol–gel auto-combustion synthesis, characterization and considering magnetic property. J Mater Sci Mater Electron 2017;28(23):17627–34.
[24] Mahdiani M, Soofivand F, Ansari F, Salavati-Niasari M. Grafting of $CuFe_{12}O_{19}$ nanoparticles on CNT and graphene: eco-friendly synthesis, characterization and photocatalytic activity. J Clean Prod 2018;176:1185–97.
[25] Shi C, Ji Y, Graham UM, Jacobs G, Crocker M, Zhang Z, et al. NO_x storage and reduction properties of model ceria-based lean NO_x trap catalysts. Appl Catal B 2012;119–120:183–96.
[26] Shinjoh H, Hatanaka M, Nagai Y, Tanabe T, Takahashi N, Yoshida T, et al. Suppression of noble metal sintering based on the support anchoring effect and its application in automotive three-way catalysis. Top Catal 2009;52:1967.
[27] Shi C, Zhang ZS, Crocker M, Xu L, Wang C, Au C, et al. Non-thermal plasma-assisted NO_x storage and reduction on a $LaMn_{0.9}Fe_{0.1}O_3$ perovskite catalyst. Catal Today 2013;211(4):96–103.
[28] Peuckert M. XPS investigation of surface oxidation layers on a platinum electrode in alkaline solution. Electrochim Acta 1984;29(10):1315–20.
[29] Zhang ZS, Chen BB, Wang XK, Xu L, Au C, Shi C, et al. NO_x storage and reduction properties of model manganese-based lean NO_x trap catalysts. Appl Catal B 2015;165:232–44.
[30] Jing L, Xu Z, Sun X, Shang J, Cai W. The surface properties and photocatalytic activities of ZnO ultrafine particles. Appl Surf Sci 2001;180(3–4):308–14.
[31] Kang M, Park ED, Kim JM, Yie JE. Manganese oxide catalysts for NO_x reduction with NH_3 at low temperatures. Appl Catal A 2007;327(2):261–9.
[32] Persson K, Ersson A, Jansson K, Fierro J, Jaras S. Influence of molar ratio on Pd–Pt catalysts for methane combustion. J Catal 2006;243(1):14–24.
[33] Infantes-Molina A, Righini L, Castoldi L, Loricera CV, Fierro JLG, Sin A, et al. Characterization and reactivity of Ce-promoted PtBa lean NO_x trap catalysts. Catal Today 2012;197(1):178–89.
[34] Lietti L, Forzatti P, Nova I, Tronconi E. NO_x storage reduction over Pt–Ba/γ-Al_2O_3 catalyst. J Catal 2001;204(1):175–91.
[35] Symalla MO, Drochner A, Vogel H, Büchel R, Pratsinis SE, Baiker A. Structure and NO_x storage behaviour of flame-made $BaCO_3$ and Pt/$BaCO_3$ nanoparticles. Appl Catal B Environ 2009;89(1–2):41–8.
[36] Broqvist P, Panas I, Grönbeck H. Toward a realistic description of NO_x storage in BaO: the aspect of $BaCO_3$. J Phys Chem B 2005;109(19):9613–21.
[37] Castoldi L, Righini L, Matarrese R, Lietti L, Forzatti P. Mechanistic aspects of the release and the reduction of NO_x stored on Pt–Ba/Al_2O_3. J Catal 2015;328:270–9.
[38] Mudiyanselage K, Weaver JF, Szanyi J. Catalytic decomposition of $Ba(NO_3)_2$ on Pt(111). J Phys Chem C 2011;115(13):5903–9.